

Identification of isotropic and orthotropic constitutive parameters by FEA-free energy-based inverse characterization method

Shen Shang^{1a}, Gun Jin Yun^{*1}, Shilpa Kunchum^{2b} and Joan Carletta^{2c}

¹Department of Civil Engineering, The University of Akron, Akron, OH, 44325, USA

²Department of Electrical & Computer Engineering, The University of Akron, Akron, OH, 44325, USA

(Received March 31, 2011, Revised January 9, 2013, Accepted January 11, 2013)

Abstract. In this paper, identification of isotropic and orthotropic linear elastic material constitutive parameters has been demonstrated by a FEA-free energy-based inverse analysis method. An important feature of the proposed method is that it requires no finite element (FE) simulation of the tested material. Full-field displacements calculated using digital image correlation (DIC) are used to compute DIC stress fields enforcing the equilibrium condition and DIC strain fields using interpolation functions. Boundary tractions and displacements are implicitly recast into an objective function that measures the energy residual of external work and internal elastic strain energy. The energy conservation principle states that the residual should be zero, and so minimizing this objective function inversely identifies the constitutive parameters. Synthetic data from simulated testing of isotropic materials and orthotropic composite materials under 2D plane stress conditions are used for verification of the proposed method. When identifying the constitutive parameters, it is beneficial to apply loadings in multiple directions, and in ways that create non-uniform stress distributions. The sensitivity of the parameter identification method to noise in both the measured full-field DIC displacements and loadings has been investigated.

Keywords: digital image correlation; constitutive law; inverse analysis; parameter identification; finite element; optimization; orthotropic material; anisotropic material

1. Introduction

In the past decade, significant progress has been made in the identification of material constitutive parameters, owing to advances in full-field displacement measurement techniques. Enriched information from the digital image correlation (DIC) technique in particular has significantly facilitated our understanding of material behavior (Regez *et al.* 2008). A recent special issue (Vol. 48 Issue 4 2008 of *Experimental Mechanics*) compiles state-of-the-art DIC techniques in various applications in experimental mechanics.

In the literature, there are five distinct categories of inverse identification methods: 1) finite element model updating (FEMU) methods (Mahnken 2000, Pagnacco *et al.* 2005, Hild and Roux

*Corresponding author, Assistant Professor, E-mail: gy3@uakron.edu

^aGraduate Student, E-mail: ssl164@zips.uakron.edu

^bGraduate Student, E-mail: sk92@zips.uakron.edu

^cAssociate Professor, E-mail: carlett@uakron.edu

2006); 2) constitutive equation gap methods (CEGM) (Constantinescu and Tardieu 2001, Geymonat and Pagano 2003, Latourte *et al.* 2008); 3) virtual field methods (VFM) (Avril *et al.* 2004, Grediac *et al.* 2006, Pierron *et al.* 2007, Avril *et al.* 2008); 4) equilibrium gap methods (EGM) (Claire *et al.* 2004, Crouzeix *et al.* 2009); and 5) the reciprocity gap method (RGM) (Calderon 1980). The existing identification methods all have in common that they enforce equilibrium conditions, that is, either in weak or strong form, the constitutive relationships that relate full-field displacements to the stresses, and either in an analytical or numerical way, the boundary conditions that are essential to all boundary value problems. However, they differ in the objective functions they use, and in whether they require measured full-field displacement or not.

As updating-based methods, the FEMU methods iteratively update constitutive parameters so as to minimize an objective function that represents the error, or gap, between a measured quantity and the same quantity computed using finite element analysis. In 2007, Avril and Pierron compared the VFM with FEMU methods based on minimization of a variety of gaps, such as displacement gap, constitutive equation gap and equilibrium gap. They concluded that FEMU based on “displacement gap” minimization yields equations that are similar to those used by the VFM (Avril and Pierron 2007). In 2008, Avril *et al.* summarized the existing parameter identification methods and compared them for the identification of linear elastic material parameters (i.e., Young’s modulus E and Poisson ratio ν) from tensile, Brazilian, shear-flexural, and biaxial tests (Avril *et al.* 2008). The FEMU approach has been applied to a variety of problems, including parameter identification for materials with linear elastic (Lecompte *et al.* 2007), viscoelastic (Moreau *et al.* 2006), elasto-plastic (Kajberg and Lindkvist 2004) and viscoplastic (Kajberg and Wikman 2007) behavior. Like the CEGM and RGM, FEMU methods do not require full-field measurements; partial measurements can be sufficient to determine the constitutive parameters. However, the FEMU methods require iterative finite element analyses, which take a great deal of computational time.

In VFM, a chosen set of kinematically admissible virtual displacement fields is assumed and substituted into the virtual work equation along with full-field displacements. This leads to a system of linear equations that is solved for constitutive parameters (Grediac and Vautrin 1990). Both VFM and EGM have the advantage of faster computation times than the previously mentioned approaches, but require full-field measurements in order to reasonably determine the constitutive parameters. Further, the VFM does not need to explicitly compute statically admissible stress fields. The equilibrium condition is implicitly enforced through using the virtual work equation.

For the past two decades, extensive studies have been conducted using the VFM approach for identification of orthotropic elastic (Chalal *et al.* 2006) and elasto-plastic (Grediac and Pierron 2006, Avril *et al.* 2008) material parameters. One of the limitations in the VFM approach is that the choice of virtual displacement fields that are kinematically admissible depends heavily on complexities of the sample geometry and stress fields within the solids, leading to the need for optimized choice of the fields (Avril *et al.* 2008). Furukawa *et al.* used incremental energy equivalence between external work and internal strain energy to identify elastic moduli of laminate composite materials under multi-axial loadings (Furukawa *et al.* 2008). From the view of optimized experimental design, they also suggested a method to find loading paths to better identify anisotropic material parameters (Furukawa and Michopoulos 2008b, a).

The proposed method is a novel inverse identification method for extracting constitutive parameters of isotropic and orthotropic materials. In the proposed method, strains are calculated from experimentally measured full-field displacements obtained by the DIC technique. Unlike the

VFM, the proposed method ensures that the stress fields computed are statically admissible. In order to identify constitutive parameters, an optimization technique is used to minimize an objective function that represents differences between the internal energy and external work. Additionally, the stress is calculated by an element-by-element FEA-free method that approximates the stress fields satisfying local equilibrium conditions. The element-by-element approach uses much less memory than finite element analysis approaches that assemble large system matrices. Using the element-by-element approach, it is possible to choose the polynomial order used for stress field approximations depending on the element size and stress gradients. The approach explicitly enforces equilibrium conditions based on the true DIC displacements. Minimization of the objective function based on the energy principle also implicitly enforces traction and displacement boundary conditions. Furthermore, the proposed method is free from additional considerations on the choice of the kinematically admissible virtual displacement field.

2. Full field displacement obtained by two-dimensional digital image correlation technique

A digital image correlation (DIC) technique is used to provide the two-dimensional full-field surface displacement needed for the proposed method. A full-field optic sensor captures images of the surface of the target. A pair of images (reference or undeformed, and deformed) are compared. Given a point on the target surface, specified by its pixel coordinates on the undeformed image, the DIC technique finds the pixel coordinates of the corresponding point in the deformed image. The displacement of the surface point is then calculated in terms of pixels, and converted to physical displacement. Full-field DIC displacement is obtained by repeating the procedure for all surface points of interest. It is worth noting that for the proposed method, DIC displacement is computed for surface points corresponding directly to the nodes in the mesh used for strain and stress calculation in Section 3.

The deformed image pixel coordinates (x', y') that match a particular point (x, y) in the undeformed image are found by comparing a region or *facet* surrounding the point with regions or *windows* of the same number of pixels in the deformed image. It is not expected that the deformed image will have a window that exactly matches a given facet, because the specimen may be stretched, compressed, or twisted. Thus, the method looks only for the window in the deformed image that best matches the facet. Displacement is measured from the middle of the facet (as indexed in the undeformed image) to the middle of the best matching window (as indexed in the deformed image). The best match is defined as the one that maximizes the correlation between the facet and the window. The correlation metric used is

$$C = \frac{\sum_{i=1}^M \sum_{j=1}^N (f_{i,j} - \mu_{\text{facet}}) \times (w_{i,j} - \mu_{\text{window}})}{\sqrt{\sum_{i=1}^M \sum_{j=1}^N (f_{i,j} - \mu_{\text{facet}})^2} \times \sqrt{\sum_{i=1}^M \sum_{j=1}^N (w_{i,j} - \mu_{\text{window}})^2}} \quad (1)$$

where both the facet and the window are of size M pixels \times N pixels, reindexed as they are cut out of their original images so that $i = 1, 2, \dots, M$ and $j = 1, 2, \dots, N$. In the formula, $f_{i,j}$ and $w_{i,j}$ denote the luminance values of pixel (i, j) from the facet and the window, respectively, and μ_{facet} and

μ_{window} denote the mean of the luminances of all the pixels in the facet and the window, respectively.

An important consideration in implementation of the DIC method is how large a zone of interest (ZOI) should be considered in computing the correlation metric. Having found an appropriate facet size, the displacement of a particular point in the undeformed image can be found by first cutting a facet out around that point in the undeformed image, and then sliding the facet over the deformed image, calculating correlation at each point, to find the point of maximum correlation. The computational complexity of the search for the point of maximum correlation is reduced by doing a local search around a probable location, rather than sliding the facet over the entire deformed image.

3. FEA-free energy-based inverse characterization method

The proposed method is applied to identification of linear elastic constitutive parameters of materials showing either isotropic or orthotropic characteristics. In addition to full-field displacement, force and displacement boundary data should be known a priori. The boundary displacements can be readily measured by LVDTs or extensometers, depending on the test setup and specimen geometry. Alternatively, the full-field image sensor can provide boundary displacements in addition to the full-field displacement. Load cells or force transducers can measure the resultant, which can then be distributed onto the boundary nodes. The load cell sensors should be triggered to capture data synchronously with the full-field optic sensor used for the DIC. In the course of laboratory (uniaxial, biaxial, or shear) testing of target materials, boundary forces and displacements can be obtained at multiple equilibrium points along the force-displacement curve directly from load cell sensors.

Fig. 1 gives a flowchart of the proposed FEA-free energy-based inverse characterization method for constitutive parameter identification. The DIC displacement is used to calculate DIC strains. Based on the DIC displacement and strain, along with boundary displacement and force data, the proposed method iteratively tunes the material parameters so as to minimize the accumulated difference between the internal and external energy. Material parameters are encoded and optimized using a steady state genetic algorithm (SSGA). The full-field displacement U_{DIC} is used in computation of stress fields using updated constitutive parameters. Keys to the proposed method are the computational procedures used to obtain DIC strains and stresses. In the following, the DIC strain and stress computation procedures are introduced in detail; these procedures follow the basic governing equations of the underlying boundary value problems.

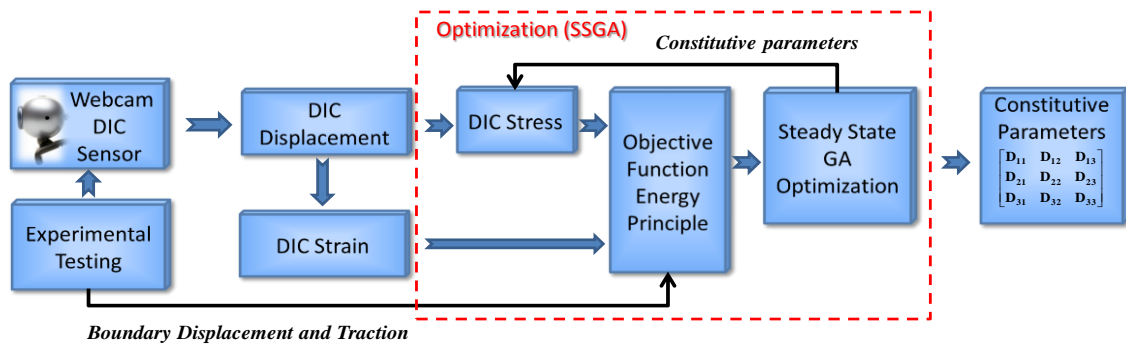


Fig. 1 Flowchart of the proposed method for constitutive parameter identification

3.1 Governing equations of boundary value problems

The governing equations of a three-dimensional solid body B with arbitrary shape under prescribed boundary tractions (τ_b) on traction boundary Ω_t and displacements (u_b) on displacement boundary Ω_u are described as

$$\begin{aligned} \operatorname{div} \boldsymbol{\sigma} + \mathbf{b} &= 0 & \text{in } B \\ \boldsymbol{\sigma} &= \lambda \operatorname{tr}(\boldsymbol{\varepsilon}) \mathbf{I} + 2\mu \boldsymbol{\varepsilon} & \text{in } B \\ \boldsymbol{\varepsilon} &= \frac{1}{2} (\mathbf{F}^T \mathbf{F} - \mathbf{I}) & \text{in } B \\ \boldsymbol{\sigma} \mathbf{n} &= \boldsymbol{\tau}_b & \text{on } \Omega_t \\ \mathbf{u} &= \mathbf{u}_b & \text{on } \Omega_u \end{aligned} \quad (2)$$

In Eq. (2), $\boldsymbol{\sigma}$ indicates the Cauchy stress tensor and \mathbf{b} indicates the body force vector acting in the volume. The second equation indicates the linear elastic stress ($\boldsymbol{\sigma}$) and strain ($\boldsymbol{\varepsilon}$) constitutive relationship in terms of Lamé constants (λ and μ). \mathbf{F} indicates the deformation gradient, and \mathbf{n} is the outward unit normal vector on the surface where the traction vector is prescribed. Considering the free surface as boundaries where the traction is zero, $\partial B = \Omega_t \cup \Omega_u$. Note that $\Omega_t \cap \Omega_u = \emptyset$. Eq. (2) has 15 unknowns: three displacement components (\mathbf{u}), six stress components ($\boldsymbol{\sigma}$), and six strain components ($\boldsymbol{\varepsilon}$). Expressing the stresses in terms of three-dimensional displacements using the constitutive relation and substituting into the equilibrium equations, a set of partial differential equations (known as Navier's equations) are expressed in Cartesian tensors using Einstein summation notation as

$$(\lambda + \mu) \frac{\partial^2 u_k}{\partial x_k \partial x_i} + \mu \frac{\partial^2 u_i}{\partial x_k \partial x_k} + b_i = 0 \quad \text{in } B \quad (3a)$$

$$\lambda \frac{\partial u_k}{\partial x_k} n_i + \mu \left(\frac{\partial u_i}{\partial x_j} + \frac{\partial u_j}{\partial x_i} \right) n_j = \tau_{bi} \quad \text{on } \Omega_t \quad (3b)$$

$$u_i = u_{bi} \quad \text{on } \Omega_u \quad (3c)$$

In constitutive parameter identification, the measured full-field displacements are considered to be true. Thus, the constitutive parameters found automatically correspond to kinematically admissible fields. However, it is more challenging to obtain constitutive parameters that correspond to statically admissible stress fields, since the stress response is determined by the displacements and constitutive parameters, but must also simultaneously satisfy local equilibrium and traction boundary conditions, as given in Eq. (3b). In the proposed DIC stress computation method, parameterization of the stress fields is accomplished in a way that ensures that the stress fields satisfy both the measured displacements and the local equilibrium conditions at every iteration used to update the constitutive parameters.

3.2 DIC strain computations

In what follows, positions are expressed in a two-dimensional Cartesian coordinate system using basis $\{\mathbf{e}_1, \mathbf{e}_2\}$. Consider a material point $\mathbf{z} = \{x, y\}$ on the surface of the undeformed

specimen, i.e., at time t_0 . After the specimen is deformed, the material point moves to a new position \mathbf{x} , expressed as

$$\mathbf{x} = \mathbf{z} + \mathbf{u}(\mathbf{z}, t), \quad t > t_0 \quad (3)$$

where $\mathbf{u} = \{u, v\}$ is the displacement vector of the material point \mathbf{z} . The deformation gradient \mathbf{F} , defined as the rate of change of deformation with respect to material point \mathbf{z} , is expressed as

$$\mathbf{F} = \nabla \mathbf{x} = \frac{\partial \mathbf{x}}{\partial \mathbf{z}} = \mathbf{I} + \nabla \mathbf{u}_{DIC} = \left(\delta_{ij} + \frac{\partial \{\mathbf{u}_{DIC}\}_i}{\partial z_j} \right) [\mathbf{e}_i \otimes \mathbf{e}_j] \quad (4)$$

where δ_{ij} is the Kronecker delta and \mathbf{I} is the identity tensor. The deformation gradient carries information on both stretch and rotation, and can be decomposed into stretch (\mathbf{U}) and rotation (\mathbf{R}) tensors by the polar decomposition ($\mathbf{F} = \mathbf{R}\mathbf{U}$).

The DIC technique provides displacement at all nodal points of the finite element (FE) mesh; the displacement fields between FE nodal points are interpolated from the DIC displacements using the eight-node isoparametric shape functions. The gradient of the in-plane full-field DIC displacement is

$$\frac{\partial \{\mathbf{u}_{DIC}\}_i}{\partial z_j} = \begin{bmatrix} \frac{\partial u}{\partial x} & \frac{\partial u}{\partial y} \\ \frac{\partial v}{\partial x} & \frac{\partial v}{\partial y} \end{bmatrix} = \begin{bmatrix} \sum \frac{\partial N_i}{\partial x} u_i & \sum \frac{\partial N_i}{\partial y} u_i \\ \sum \frac{\partial N_i}{\partial x} v_i & \sum \frac{\partial N_i}{\partial y} v_i \end{bmatrix} \quad (5)$$

where N_i is the standard shape function of the eight-node finite element in isoparametric coordinates, given by

$$\begin{aligned} N_1 &= \frac{1}{4}(1-\xi)(1-\eta) - \frac{1}{2}\left(\frac{1}{2}(1-\xi)(1-\eta^2) + \frac{1}{2}(1-\xi^2)(1-\eta)\right) \\ N_2 &= \frac{1}{4}(1+\xi)(1-\eta) - \frac{1}{2}\left(\frac{1}{2}(1-\xi^2)(1-\eta) + \frac{1}{2}(1+\xi)(1-\eta^2)\right) \\ N_3 &= \frac{1}{4}(1+\xi)(1+\eta) - \frac{1}{2}\left(\frac{1}{2}(1+\xi)(1-\eta^2) + \frac{1}{2}(1-\xi^2)(1+\eta)\right) \\ N_4 &= \frac{1}{4}(1-\xi)(1+\eta) - \frac{1}{2}\left(\frac{1}{2}(1-\xi^2)(1+\eta) + \frac{1}{2}(1-\xi)(1-\eta^2)\right) \\ N_5 &= \frac{1}{2}(1-\xi^2)(1-\eta) \\ N_6 &= \frac{1}{2}(1+\xi)(1-\eta^2) \\ N_7 &= \frac{1}{2}(1-\xi^2)(1+\eta) \\ N_8 &= \frac{1}{2}(1-\xi)(1-\eta^2) \end{aligned} \quad (6)$$

where ξ and η indicate the isoparametric coordinates. Hence, using the determined $\{\mathbf{u}_{DIC}\}_i$, the Green strain tensor $\{\boldsymbol{\varepsilon}_{DIC}\}_{ij}$ is computed as

$$\{\boldsymbol{\varepsilon}_{DIC}\} = \frac{1}{2}[\mathbf{F}^T(\mathbf{z}, t)\mathbf{F}(\mathbf{z}, t) - \mathbf{I}] \quad (7)$$

Strains at the Gauss points are directly calculated from the deformation gradients $[\mathbf{F}]$ as shown in Eq. (7).

Any artificial rigid body motion (translational, rotational or a combination of the two) introduced when the web camera or test equipment is disturbed during a test is eliminated by the method, so that only pure deformations are considered. This is true because the eigenvalues of the Green deformation tensor $\mathbf{C} = \mathbf{F}^T\mathbf{F} = \mathbf{U}^T\mathbf{U}$ correspond to the squares of stretch. To verify the immunity to rigid body motions, rigid body motions were added to a full-field displacement computed from a simulated uniaxial tension test of the specimen that is same as the one used in Section 5.1. The applied displacement boundary condition is 0.05 mm on the right boundary of the specimen in the 1-1 direction. The proposed DIC strain computation procedures were followed to compute the Green strains. Fig. 2 compares the contour plots of the longitudinal strain as given by the DIC strain computations with a reference strain calculated from a pure deformation using ABAQUS. The DIC strain matches the reference strain.

3.3 DIC stress computations

Use of an element-by-element method for computing stress given the DIC displacements is suggested. Although Latourte *et al.* (2008) also used a set of statically admissible functions to project the stress field (enforcing equilibrium) (Latourte *et al.* 2008), their stress computation procedure is very different from that of the proposed method. In Latourte *et al.* (2008), a naturally equilibrated Airy function was chosen for enforcing equilibrium. In contrast, the proposed method enforces the equilibrium by selecting polynomial terms that satisfy both the strong form of the equilibrium equations and the nodal force equilibrium conditions. The DIC stress computation technique was originally developed as an alternative method for stress extrapolations in post-processing of finite element simulation results (Wilson and Ibrahimbegovic 1990). As previously mentioned, the DIC stress calculation is a surrogate for finite element model updating techniques; in other words, with the proposed method there is no need to perform FE simulation repeatedly using the iteratively updated constitutive parameters. Thus, the method is an FEA-free method. To ensure that the stress fields satisfy the strong form equilibrium conditions (e.g., $\sigma_{ij,j} = 0$ with no body forces), the polynomials for the stress field are determined from the Navier's equation. Interpolation functions and numerical integration methods commonly used in finite element methods are utilized.

On the condition that the FE mesh is sufficiently fine, linear polynomials are used to approximate the stress field, so that the stress field is assumed to take the form

$$\{\boldsymbol{\sigma}_{DIC}\} = [\mathbf{P}]\{\boldsymbol{\beta}\} \quad (8)$$

where $\{\boldsymbol{\beta}\} = \{\beta_1 \ \beta_2 \ \beta_3 \ \beta_4 \ \beta_5 \ \beta_6 \ \beta_7\}^T$ is the polynomial coefficient vector to be solved for each element. $[\mathbf{P}]$ is the polynomial approximation of the stress field and derived based on the general displacement field as

$$\begin{aligned} u &= a_1 + a_2 x_1 + a_3 x_2 + a_4 x_1 x_2 \\ v &= a_5 + a_6 x_1 + a_7 x_2 + a_8 x_1 x_2 \end{aligned} \quad (9)$$

This 2D displacement field contains a quadratic term $x_1 x_2$, but x_1^2 and x_2^2 are absent. $[\mathbf{P}]$ is a function of the coordinates whose form satisfies the partial differential equilibrium equations. The 2D in-plane equilibrium equation in the absence of body force is

$$\begin{aligned} \frac{\partial \sigma_{11}}{\partial x_1} + \frac{\partial \sigma_{12}}{\partial x_2} &= 0 \\ \frac{\partial \sigma_{11}}{\partial x_1} + \frac{\partial \sigma_{12}}{\partial x_2} &= 0 \end{aligned} \quad (10)$$

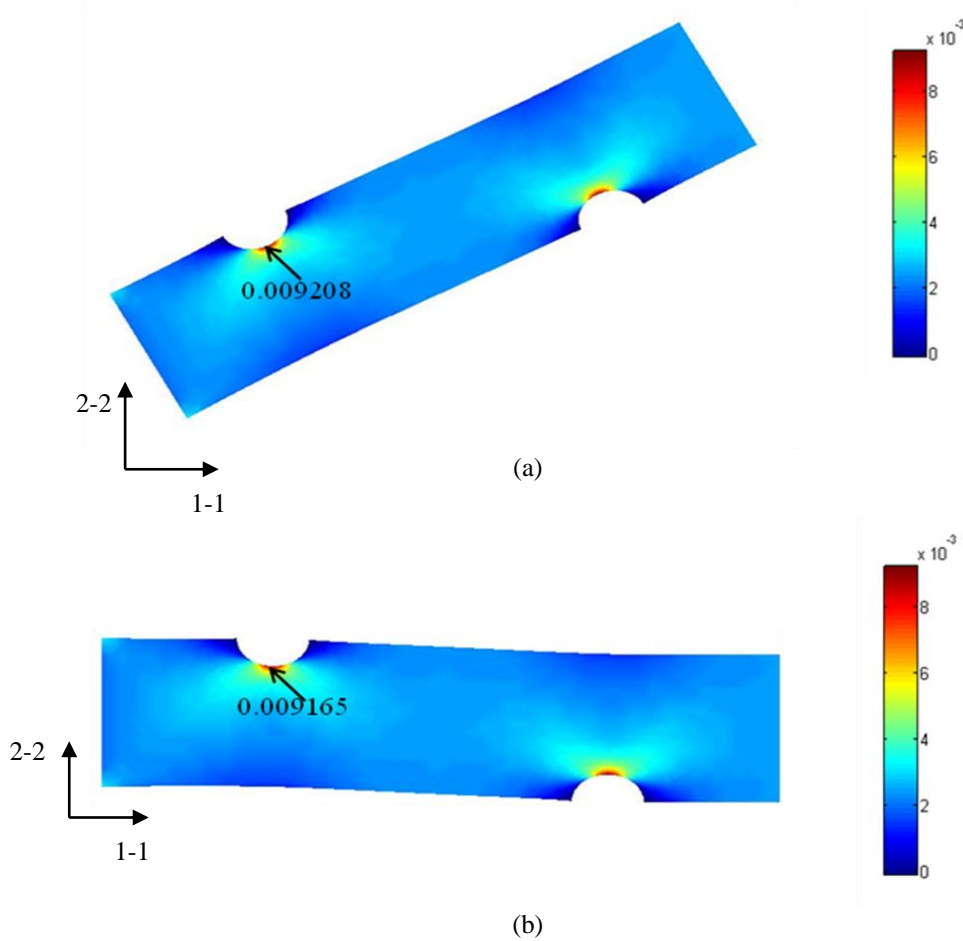


Fig. 2 Comparison of contour plots of longitudinal strain in a simulated test: (a) DIC strain, computed in MATLAB with rigid body motions added to the full-field displacement; (b) reference strain, from ABAQUS

For an infinitesimal deformation, the displacement-strain relationship of the plane stress case is

$$\begin{aligned}\varepsilon_{11} &= \frac{\partial u}{\partial x_1} = a_2 + a_4 x_2; \varepsilon_{22} = \frac{\partial v}{\partial x_2} = a_7 + a_8 x_1; \\ \varepsilon_{33} &= -\frac{\lambda}{\lambda + 2\mu}(a_2 + a_7 + a_8 x_1 + a_4 x_2); \varepsilon_{12} = \frac{1}{2}(a_3 + a_6 + a_4 x_1 + a_8 x_2)\end{aligned}\quad (11)$$

Stress can be expressed in terms of strain by applying Hooke's law

$$\boldsymbol{\sigma} = \lambda \text{tr}(\boldsymbol{\varepsilon})\mathbf{I} + 2\mu\boldsymbol{\varepsilon} \quad (12)$$

After substituting Eqs. (11) and (12) into Eq. (10), and rearranging the coefficients, one can obtain

$$\begin{aligned}\sigma_{11} &= \beta_1 + \beta_2 x + \beta_3 y \\ \sigma_{22} &= \beta_4 + \beta_5 x + \beta_6 y \\ \sigma_{12} &= \beta_7 + \beta_8 x + \beta_9 y\end{aligned}\quad (13)$$

Substituting Eq. (13) back to Eq. (10), one can easily obtain

$$\beta_9 = -\beta_2; \beta_8 = -\beta_6 \quad (14)$$

Therefore, we can find the following final form of Eq. (8)

$$\begin{bmatrix} \sigma_{11} \\ \sigma_{22} \\ \sigma_{12} \end{bmatrix} = \begin{bmatrix} 1 & x & y & 0 & 0 & 0 & 0 \\ 0 & 0 & 0 & 1 & x & y & 0 \\ 0 & -y & 0 & 0 & 0 & -x & 1 \end{bmatrix} [\beta_1 \ \beta_2 \ \beta_3 \ \beta_4 \ \beta_5 \ \beta_6 \ \beta_7]^T \quad (15)$$

$[\mathbf{P}]$ is evaluated at each Gauss point within the element. To determine $\{\boldsymbol{\beta}\}$, the nodal equilibrium condition $\{\mathbf{r}\} + \{\mathbf{r}_e\} = 0$ should be used, where $\{\mathbf{r}\} = [\mathbf{k}]_e \{\mathbf{u}_{DIC}\}$. Using standard finite element techniques, the nodal force vector $\{\mathbf{r}\}$ is computed for each finite element using the updated constitutive parameters in the $[\mathbf{D}]$ matrix. The $[\mathbf{k}]_e$ is calculated using the full Gauss numerical integration scheme in the isoparametric coordinates

$$\{\mathbf{r}\} = [\mathbf{k}]_e \{\mathbf{u}_{DIC}\} = \int_{V_e} [\mathbf{B}]^T [\mathbf{D}] [\mathbf{B}] dV \{\mathbf{u}_{DIC}\} \quad (16)$$

where $[\mathbf{B}]$ is the strain-displacement matrix and $[\mathbf{D}]$ is the material stiffness matrix, which is assumed initially and updated in an optimization process to be explained in Section 4. From the statically admissible stress fields derived in Eq. (15), the approximated nodal resisting force vector is computed as follows.

$$\{\mathbf{r}_e\} = - \int_{V_e} [\mathbf{B}]^T \{\boldsymbol{\sigma}_{DIC}\} dV_e = - \int_{V_e} [\mathbf{B}]^T [\mathbf{P}] dV_e \{\boldsymbol{\beta}\} = [\mathbf{Q}] \{\boldsymbol{\beta}\} \quad (17)$$

$$\text{where } [\mathbf{Q}] = \int_{V_e} [\mathbf{B}]^T [\mathbf{P}] dV_e \quad (18)$$

Substituting Eqs. (16) and (17) into the local equilibrium equation, the local nodal force equilibrium condition is expressed as

$$[\mathbf{Q}]\{\boldsymbol{\beta}\} = [\mathbf{k}_e]\{\mathbf{u}_{DIC}\} \quad (19)$$

Premultiplying Eq. (19) by $[\mathbf{Q}]^T$, the coefficient vector $\{\boldsymbol{\beta}\}$ can be solved for each element. The polynomial coefficient vector $\{\boldsymbol{\beta}\}$ is computed in Eq. (20) and can be substituted back into Eq. (15) to obtain the final DIC stress fields $\{\boldsymbol{\sigma}_{DIC}\}$.

$$\{\boldsymbol{\beta}\} = ([\mathbf{Q}]^T [\mathbf{Q}])^{-1} [\mathbf{Q}]^T [\mathbf{k}_e] \{\mathbf{u}_{DIC}\} \quad (20)$$

Based on the formulation, $\{\boldsymbol{\sigma}_{DIC}\}$ becomes a function of the material parameters in the $[\mathbf{D}]$ matrix. The advantage of this formulation is that the calculated stress possesses more accuracy because the equilibrium equation is applied to each element. It is also worth noting that this FEA-free method is relatively computationally efficient because it does not require calculating and taking the inverse of a large global stiffness matrix. Fig. 3 depicts the computational procedure for obtaining the DIC stress field from the DIC full-field displacements.

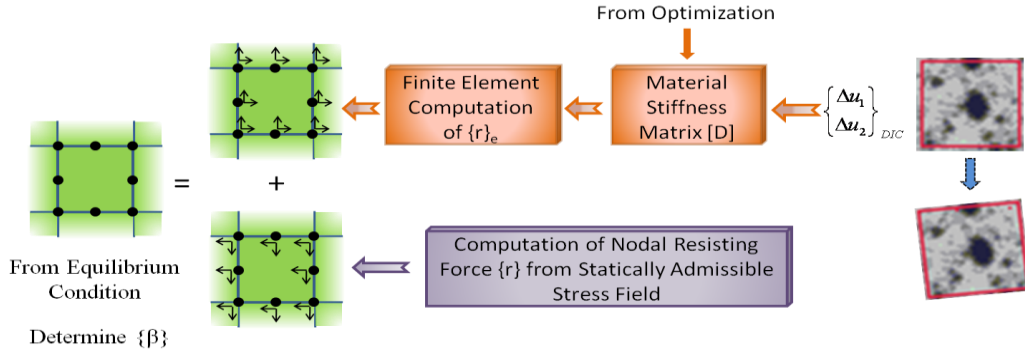


Fig. 3 Computational procedure for DIC stress computation

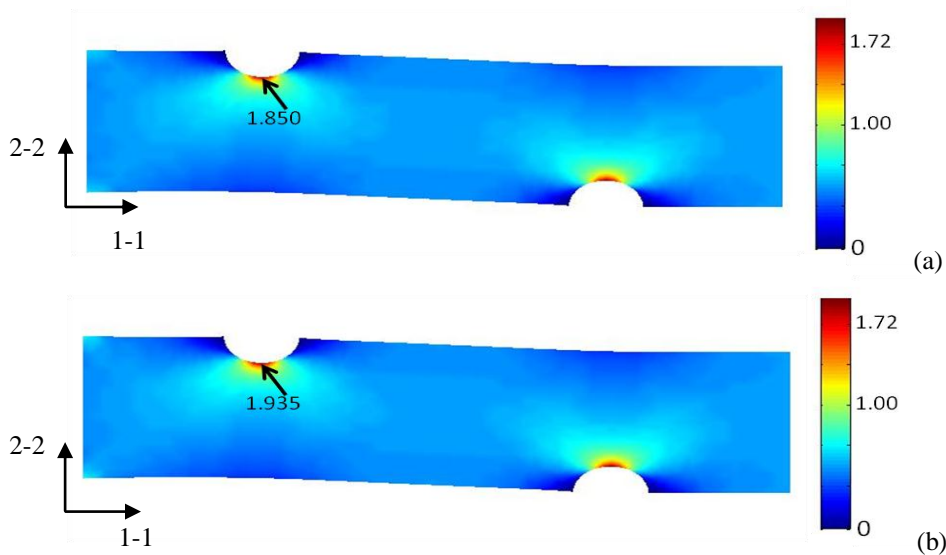


Fig. 4 Comparison of contour plots of 1-1 component of stress σ_{11} (GPa) in a simulated test: (a) DIC stress, computed in MATLAB; (b) reference stress, from ABAQUS

To verify the DIC stress computation, a simulated uniaxial tension test of the specimen that is the same as the one used in Section 5.1 is used, and results from the DIC stress computation are compared to a reference stress calculated using ABAQUS. The applied displacement boundary condition is 0.05 mm at the right boundary of the specimen in the 1-1 direction. As shown in Fig. 4, the stress field calculated using the proposed DIC stress computation method is reasonably consistent with the reference stress field; there is a slight difference in the region where the stress is concentrated.

4. Optimization method

As described in Section 3.3, the DIC stress computation procedure ensures that the equilibrium equation and constitutive law in the boundary value problems described in Eq. (2) are satisfied. However, the other two natural and essential boundary conditions in Eq. (2) remain as conditions that must be satisfied. In this paper, these boundary conditions are recast using the principle of energy conservation. The energy conservation principle allows formulation of an optimization problem that minimizes the accumulated difference between internal and external energy. Within the optimization routine, the traction and displacement boundary conditions can be implicitly enforced by including them in the objective function as follows

$$f([\mathbf{D}]) = \sum_{k=1}^{LS} \left(1 - \frac{\sum_{i=1}^{nelem} \int_{V_e} \boldsymbol{\sigma}_{DIC}^k : \boldsymbol{\varepsilon}_{DIC}^k dV_e}{\int_{\Omega_s} \mathbf{T}^k \cdot \mathbf{U}^k dS} \right)^2 ; \quad [\mathbf{D}] = \begin{bmatrix} D_{11} & D_{12} & D_{13} \\ D_{12} & D_{22} & D_{23} \\ D_{13} & D_{23} & D_{33} \end{bmatrix} \quad (21)$$

where $\boldsymbol{\sigma}_{DIC}$ and $\boldsymbol{\varepsilon}_{DIC}$ are the computed DIC stresses and strains, respectively; \mathbf{T}^k and \mathbf{U}^k are the traction and boundary displacement vectors on the boundary surface Ω_s at the k^{th} load step, and LS indicates the total number of load steps.

A steady state genetic algorithm (SSGA) is employed to search for the best set of constitutive parameters. There is a unique advantage of the SSGA: it shows searching capability comparable in terms of accuracy to other genetic algorithms, but at much faster computing speeds. The faster speed is due to the fact that the objective function needs to be evaluated for only two best solution candidates in each generation, whereas other genetic algorithms need to evaluate the objective function for all solution candidates (Yun *et al.* 2009). Depending on the directional property of the material, the number of material stiffness values to be identified varies. For example, if the material is assumed to be fully 2D anisotropic, a total of six constitutive parameters (D_{ij} : $i, j = 1, 2, 6$ and $D_{ij} = D_{ji}$) are encoded as binary strings in the SSGA optimization. However, if the material is assumed to be orthotropic, a total of four engineering material properties (E_1 , E_2 , G_{12} and ν_{12}) are encoded.

5. Numerical verification using synthetic full-field displacements

Two simulation-based experiments were done to verify the proposed method. As previously described, application of the proposed method requires that three different types of experimental

data be acquired: 1) global force on the boundary of the specimen, 2) global displacement on the boundary of the specimen, and 3) full-field displacement. The loading data can be acquired directly from the load cells, and both the boundary and full-field displacements can be derived from the images captured by the full-field optics sensor. This paper shows verification tests based on simulation, rather than experiment; thus, synthetic data from finite element simulations that use reference (true) constitutive parameters take the place of experimental data.

It is notable that the proposed method is suitable for use with anisotropic materials due to its robustness in the identification of constitutive parameters. The method developed herein is capable of determining general constitutive parameters from multiple loading stages. In the first simulation experiment, isotropic material under non-uniform stress is tested under uniaxial tension loading. Although the material is isotropic, no a priori knowledge about the material is assumed in the experiment; that is, for the purposes of identification the material is assumed to be anisotropic. In the second example, orthotropic composite material specimens with different geometries are subjected to different loadings to investigate effects of non-uniform stresses and loading direction on the performance of the identification method. Experimental noise and error in DIC displacements and boundary tractions are also considered, to investigate their effects on the performance of the proposed method.

5.1 Isotropic material under uniaxial loading and non-uniform stress states

The first experiment to verify the proposed method uses a non-conventional test specimen with two asymmetric semi-circular notches, as shown in Fig. 5; the experiment is designed specifically to generate local non-uniform strain and stress fields. Force-driven FE simulation was used to produce synthetic full-field displacement data. The FE model was fixed at the left boundary, and a uniaxial quasi-static tension test under a uniformly distributed loading of 70 kips/in² applied at the right boundary of the specimen was simulated. For this loading, the specimen is in the linear elastic region. The full-field displacement was obtained numerically by using a priori parameter set $[D_t]$ that consists of true values. The FE model is constructed as a two-dimensional plane stress problem. Thus, the terms in the $[D_t]$ matrix that are related to the z direction were set to zero for the FE simulation.

For application of the proposed method, no assumption was made about symmetry of the constitutive material matrix $[D]$; thus, the method is fully general in that it treats the material as a 2D anisotropic linear elastic material, and five constitutive stiffness values (D_{11} , D_{12} , D_{21} , D_{22} , and D_{66}) are parameterized in the inverse identification, assuming the decoupling between normal and shear components that is attributable to existence of one plane of symmetry as in monoclinic material. In this example, only one load step is used to test the proposed method, since in linear elasticity all deformation stages are proportional. However, in actual experimental testing, in order to reduce the noise effect we anticipate using multiple loading steps along the equilibrium path to gather data for use in parameter identification.

The SSGA optimization algorithm starts with an initial population of 50 solution candidates, generated by randomly choosing values in binary form for the elements of the $[D]$ matrix in such a way that the values fall between the preset upper and lower bounds shown in Table 1. In each generation of the algorithm, a 90% crossover rate and a 30% mutation rate are used to breed a new generation of solution candidates; in each generation, the best two new solutions are chosen for crossover, and the offspring replaces the two worst solutions of the previous generation. The algorithm is terminated when the 3000th generation is reached. The absolute error of the final solution is summarized in Table 1.

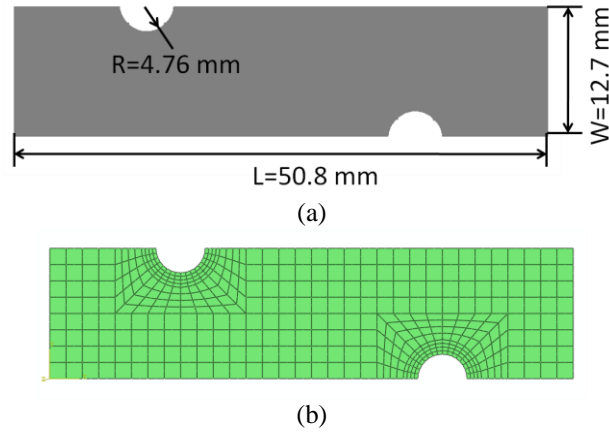


Fig. 5(a) Test specimen with semi-circular notch (thickness $t=4.76$ mm) and (b) finite element mesh for an identification model

In this verification experiment, the proposed method successfully identifies all constitutive parameters. The differences between the reconstructed values and the true values are observed to decrease as the number of generations increases, and the values of the reconstructed parameters all converge to within an acceptable error with respect to the true values. In particular, the two terms D_{11} and D_{66} were identified with error less than 2% (1.32% and 0.8%, respectively). It is natural that these two parameters are particularly well-identified, since the specimen is under dominant stress and strain distributions in the longitudinal direction, and the semi-circular notch generates high shear stress distributions around the circular notch. In comparison, the terms D_{12} , D_{21} and D_{22} showed relatively large errors, of 7.64%, 10.36% and 14.54%, respectively. Fig. 6 compares stresses simulated using the identified and true parameters; there is good agreement in all three stress component fields (S_{11} , S_{22} and S_{12}). The results of the verification experiment are promising, in that they show that the proposed method can reproduce the material behavior even from a uniaxial tension test with a single incremental load step.

Table 1 Identified parameter set and error assessment

Parameters	D_{11} (GPa)	D_{12} (GPa)	D_{21} (GPa)	D_{22} (GPa)	D_{66} (GPa)
True value	159.110	47.733	47.733	159.110	55.688
Initial upper bound	206.843	62.053	62.053	206.843	82.737
Initial lower bound	68.948	20.684	20.684	68.948	27.579
Optimized value	157.000	44.084	52.681	182.244	56.136
Error (%)	1.32	7.64	10.36	14.54	0.80

5.2 Orthotropic composite material under different loading scenarios

5.2.1 Open-hole test with single load step

A second set of verification simulations is carried out using a composite material with assumed

parameters $E_1 = 30$ (GPa), $E_2 = 5.4$ (GPa), $\mu_{12} = 0.07$, $\mu_{21} = 0.39$, and $G_{12} = 2.62$ (GPa). Two specimens with different geometries, both with a thickness of 4.76 mm, are used to verify the proposed method. The specimen geometry and loading direction influences the non-uniformity of the stress and strain fields. Determining optimal loading paths and geometries is an open problem that all inverse identification methods face (Furukawa and Michopoulos 2008a, Furukawa and Michopoulos 2008b); this problem lies out of the scope of this paper, and is not fully addressed here. Our motivation in investigating specimens with different geometries, boundary conditions and loadings, is two-fold: 1) to find a way to reduce the number of loading scenarios needed to identify a material's properties, and 2) to test the stability of the proposed method.

For this verification experiment, synthetic data was produced using displacement-controlled FE analysis; synthetic full-field displacements and boundary force data was derived. For the displacements used, the specimens were within the linear elastic region. In each test, the SSGA optimization started with solutions that were randomly generated with constitutive parameter values within preset upper and lower bounds; the bounds for a parameter were placed 50% above and below the true value. In each generation of the SSGA, a 90% crossover rate and a 30% mutation rate are used. The optimization was terminated when the 6,000th generation is reached. The objective function used is the one shown in Eq. (21), with the symmetry condition ($D_{12} = D_{21}$) and with assumed orthotropic behavior ($D_{16} = D_{61} = 0.0$, $D_{26} = D_{62} = 0.0$). As a result, four parameters (D_{11} , D_{22} , D_{12} and D_{66}) are to be identified.

In case one, a 76.2 mm by 50.8 mm open-hole coupon test specimen with a 15.24 mm diameter hole is loaded under two loading scenarios: a) shear loading on the right edge and b) transverse tension loading on the top edge. For each loading scenario, a single load step is used to provide the

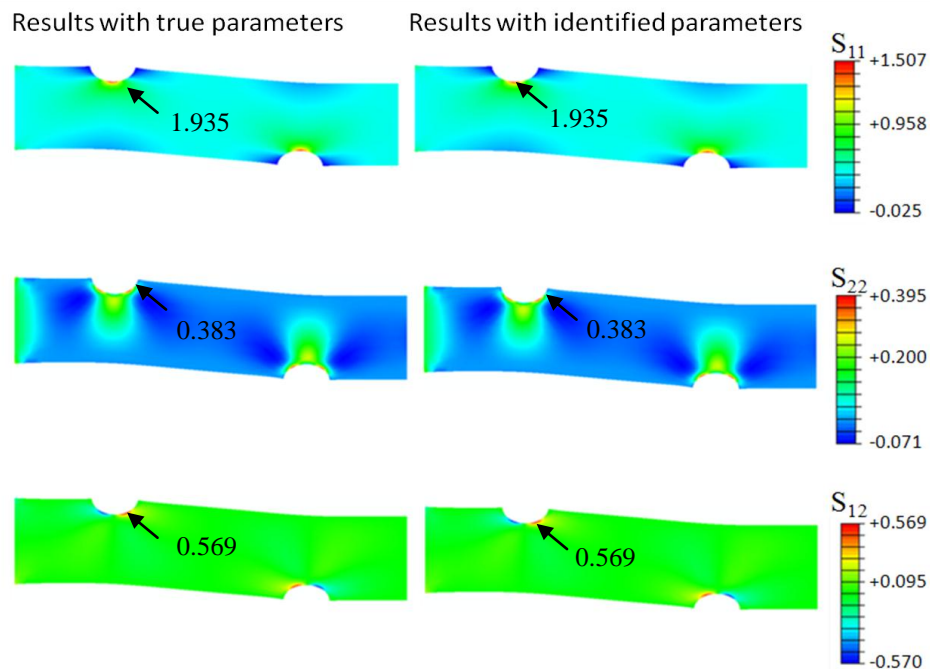


Fig. 6 Comparison of stress (GPa) components for identified material properties and reference material properties

Table 2 Identification results of case one: open-hole coupon case

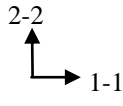
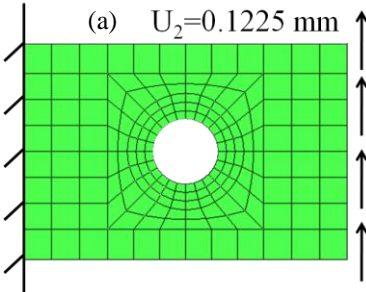
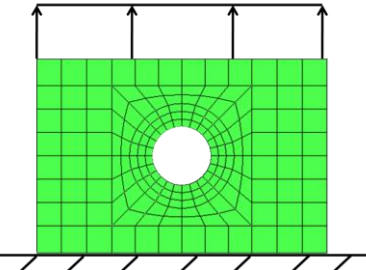
Boundary	Material Matrix (GPa)	Error (%)
	$\mathbf{D}_T = \begin{bmatrix} 30.845 & 2.166 & 0 \\ 2.166 & 5.552 & 0 \\ 0 & 0 & 2.620 \end{bmatrix}$	N/A
(a) $U_2=0.1225$ mm 	$\mathbf{D}_I = \begin{bmatrix} \boxed{31.350} & 1.680 & 0 \\ 1.680 & 7.130 & 0 \\ 0 & 0 & \boxed{2.570} \end{bmatrix}$	$\mathbf{e} = \begin{bmatrix} \boxed{1.64} & 22.41 & 0 \\ 22.41 & 28.41 & 0 \\ 0 & 0 & \boxed{1.91} \end{bmatrix}$
(b) $U_2=0.098$ mm 	$\mathbf{D}_I = \begin{bmatrix} 39.480 & 2.880 & 0 \\ 2.880 & \boxed{5.600} & 0 \\ 0 & 0 & 1.450 \end{bmatrix}$	$\mathbf{e} = \begin{bmatrix} 27.99 & 32.98 & 0 \\ 32.98 & \boxed{0.86} & 0 \\ 0 & 0 & 44.65 \end{bmatrix}$
Composed Results	$\mathbf{D}_I = \begin{bmatrix} 31.350 & 1.680 & 0 \\ 1.680 & 5.600 & 0 \\ 0 & 0 & 2.570 \end{bmatrix}$	$\mathbf{e} = \begin{bmatrix} 1.64 & 22.41 & 0 \\ 22.41 & 0.86 & 0 \\ 0 & 0 & 1.91 \end{bmatrix}$

Table 3 Engineering material properties as calculated using identified parameters

	E_1 (GPa)	E_2 (GPa)	G_{12} (GPa)	μ_{12}	μ_{21}
True Value	30.001	5.400	2.620	0.070	0.390
Identified	30.847	5.510	2.570	0.054	0.300
Error (%)	2.82	2.034	1.92	22.86	23.08

reference data. The boundary conditions, loading directions, geometry of the specimen, true material matrix \mathbf{D}_T , identified material matrix \mathbf{D}_I and absolute final error \mathbf{e} in the identified material matrix are summarized in Table 2. Parameters marked by the green box are identified successfully. The first loading scenario allows for successful identification of parameters D_{11} and D_{66} ; the second loading scenario allows for successful identification of parameter D_{22} . Therefore, by composing results from the two loading scenarios, taking D_{11} , D_{12} and D_{66} as identified using the first loading scenario, and D_{22} as identified using the second, it is possible to identify all

parameters except D_{12} with acceptable error. The engineering material properties E_1 , E_2 , μ_{21} and G_{12} are also back-calculated based on the identified material matrix. The property μ_{12} is calculated using the symmetric condition, $\mu_{21}/E_1 = \mu_{12}/E_2$. The absolute error between the identified value and the true value for each engineering material property is listed in Table 3. E_1 , E_2 and G_{12} were identified with high accuracy.

Since the proposed method is formulated in such a way that the error between the external and internal energies is minimized, insight into the effectiveness of a particular loading scenario can be gained by considering the energy distribution associated with directional deformations. These are given as

$$W_{ext} = \int_{\Omega_S} \mathbf{T}^k \cdot \mathbf{U}^k dS \quad (22)$$

$$\begin{aligned} W_{int} &= \sum_{i=1}^{nelem} \int_{V_e} \boldsymbol{\sigma}^k : \boldsymbol{\varepsilon}^k dV_e = \sum_{i=1}^{nelem} \int_{V_e} [(D_{11}\varepsilon_{11}^2) + (D_{22}\varepsilon_{22}^2) + (D_{66}\varepsilon_{33}^2) + 2(D_{12}\varepsilon_{11}\varepsilon_{22})] dV_e \\ &= W_{11} + W_{22} + W_{33} + W_{12} \end{aligned} \quad (23)$$

Eq. (23) shows that the internal energy has four components corresponding to the four constitutive parameters D_{11} , D_{22} , D_{66} , and D_{12} . It is clear that the relative size of an energy component plays a role in how well the corresponding constitutive parameter can be identified. The percentages of each energy component are plotted in Fig. 7 for the two loading scenarios. In the case of pure shear loading, stress components, σ_{11} and σ_{33} are dominant due to bending and shearing actions as seen in Fig. 7(a). It is expected, then, as seen in Table 2, that D_{11} and D_{66} could be identified. In the case of uniaxial tension loading in 2-2 direction, only D_{22} could be identified successfully; this is expected, since, as shown in Fig. 7(b), the energy component in the 2-2 direction is dominant.

From this analysis of the performance of the identification, it can be seen that each loading scenario can identify some of the parameters in the material constitutive matrix. The complete set of parameter values can be successfully identified by changing the loading direction and combining all the results from the different loading scenarios. Both D_{12} and μ_{21} have large error because neither of the two in loading scenarios used has a significant W_{12} energy component. In order to increase W_{12} , both ε_{11} and ε_{22} have to be increased. Further experiments show that balanced distribution of the energy components can significantly increase the performance of the proposed method. To demonstrate this, we next investigate a quarter of the open-hole specimen under multi-axial and non-proportional loadings.

5.2.2 Open-hole test specimen under non-proportional biaxial tension-compression loading condition

In this next verification case, a non-proportional biaxial loading is applied to a 50.8 mm by 50.8 mm specimen with an arch notch at the corner. Fig. 8(a) shows the geometry of the specimen, the symmetric boundary conditions, and the loading directions. The non-proportional loading path is depicted in Fig. 8(b). The reference engineering material properties are $E_1 = 30.000$ (GPa), $E_2 = 24.000$ (GPa), $\mu_{12} = 0.16$, $\mu_{21} = 0.2$, $G_{12} = 5.000$ (GPa). A displacement-controlled FE analysis was conducted to produce synthetic data in the same way as used in the previous case, except that a total of nine loading steps are included in this case. In the SSGA optimization process, the initial upper and lower bound errors, the total number of generations, the crossover rate, and the mutation rate are set to be the same as in the previous case. Fig. 9 shows the converged objective function value after 6000 iterations.

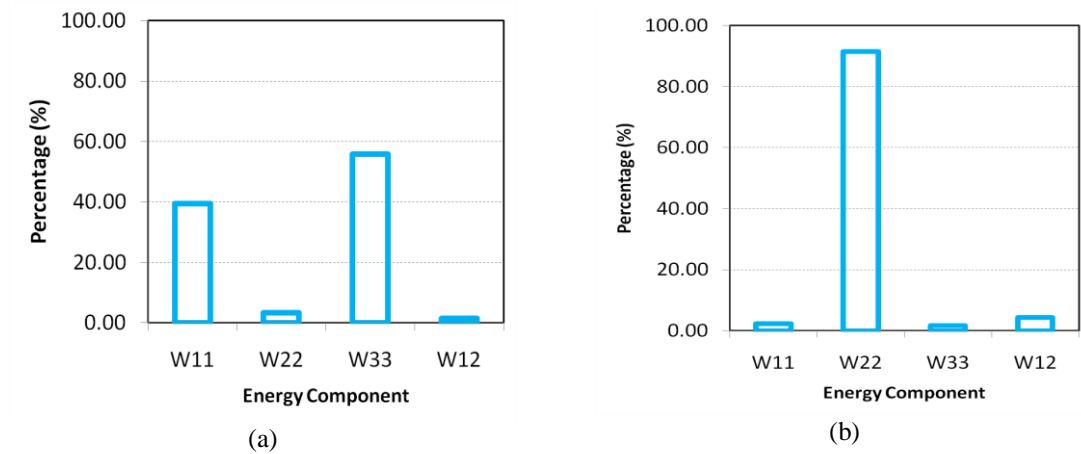


Fig. 7 Energy component percentages: (a) pure shear loading case, (b) uniaxial tension loading in 2-2 direction

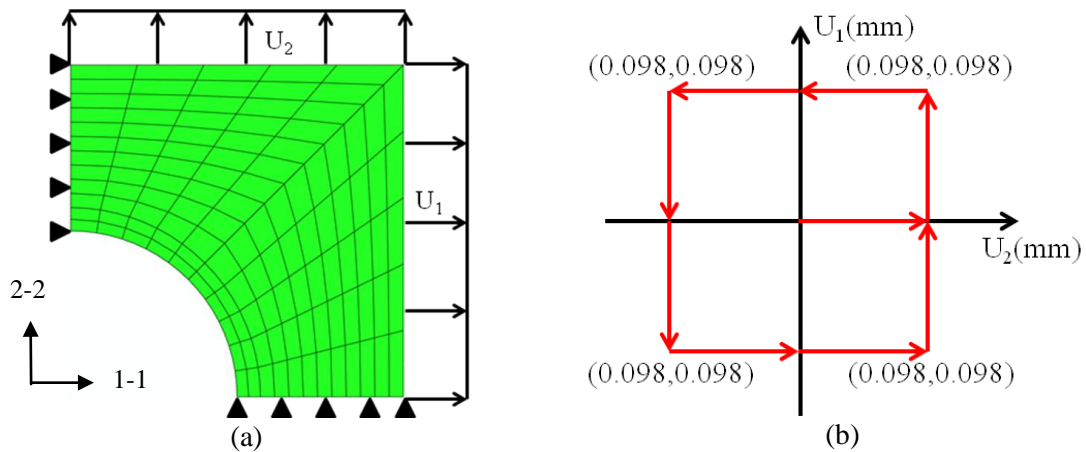


Fig. 8 (a) FE model of the specimen with symmetric boundary conditions and (b) applied non-proportional loading path

Table 4 Identification results of case two: biaxial loading case

Boundary Traction		Material Matrix (GPa)			Error (%)
True Material Matrix	$\mathbf{D}_T =$	$\begin{bmatrix} 30.991 & 4.895 & 0 \\ 4.895 & 23.414 & 0 \\ 0 & 0 & 5.000 \end{bmatrix}$			N/A
Identified Material Matrix	$\mathbf{D}_I =$	$\begin{bmatrix} 31.080 & 5.229 & 0 \\ 5.229 & 24.859 & 0 \\ 0 & 0 & 4.611 \end{bmatrix}$			$\mathbf{e} = \begin{bmatrix} 0.29 & 5.45 & 0 \\ 5.45 & 0.27 & 0 \\ 0 & 0 & 7.78 \end{bmatrix}$

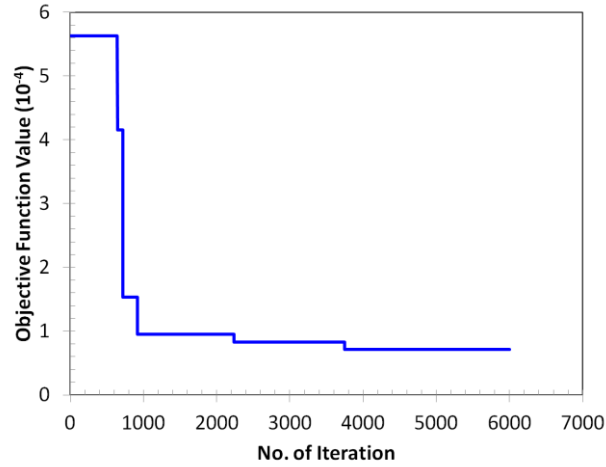


Fig. 9 Objective function values vs. No. of iterations

Table 5 Identification results of engineering material properties

	E_1 (GPa)	E_2 (GPa)	G_{12} (GPa)	μ_{12}	μ_{21}
True Value	30.000	24.000	5.000	0.160	0.200
Identified	29.981	23.980	4.611	0.168	0.210
Error (%)	0.07	0.08	7.78	4.98	5.17

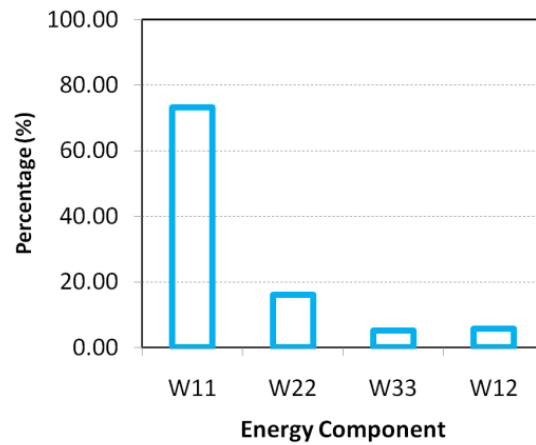


Fig. 10 Energy component percentage of the biaxial load case

As before, the internal energy computed by using DIC stresses and DIC strains during the nine loading steps are used in the objective function to identify the material parameters. For this case, all parameters are identified successfully; each parameter has an acceptable error with respect to the corresponding true value (See Table 4). The non-proportional biaxial tension-compression test used generates multi-stress states at every material point within the specimen. Moreover, due to

the geometry of the specimen, considerable shear stresses are developed even though only tension-compression loading is applied. As shown in Fig. 10, the internal energy components are relatively better balanced than in the previous case; in particular, the relative size of energy component W_{12} is significantly larger, resulting in improved identification of D_{12} . When the identified material parameters are used to backcalculate the engineering material properties, elastic moduli E_1 and E_2 are identified with errors less than 0.1%. The Poisson ratio μ_{21} and shear modulus G_{12} were also identified with acceptable errors, 5.17% and 7.78%, respectively (See Table 5). According to the results from this example, the non-proportional loading with measurements at multiple loading steps and non-uniform stress states are clearly beneficial in identifying material stiffness values.

Fig. 11 compares S_{11} , S_{22} , and S_{12} stress (GPa) contours at the second load step for three sets of material parameters: initial parameters at the lower bound of the parameter sets used at the start of the SSGA optimization, the identified material parameters, and the true parameters. The reconstructed stress field using the identified material stiffness parameters is clearly consistent with the reference stress field.

Comparing with traditional material characterization methods using strain gages, the proposed method has advantages in the fact that it can utilize full-field displacements from the noncontact DIC sensing technique. It is notable that strain gages can provide only localized strain values at a limited number of locations. Moreover, accuracy of the measured strains could vary depending on the quality of installation. In contrast, the proposed method allows for better estimation of the tested material's constitutive parameters, owing to the additional information provided by the full-field displacement, stress, and strain data obtained via digital image correlation (DIC).

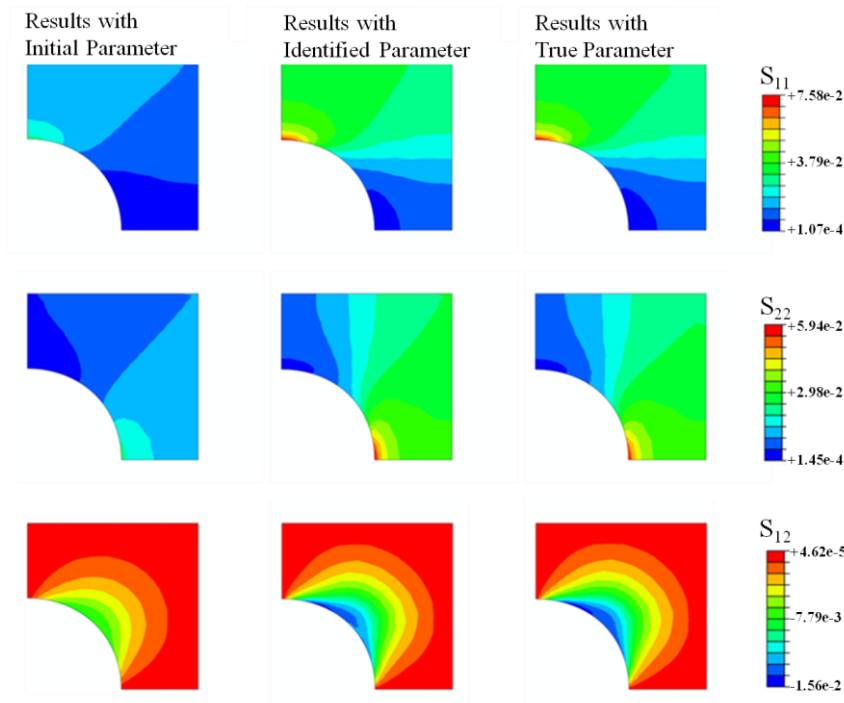


Fig. 11 Comparison of the stress contours at second loading step for simulations using initial, identified and true material parameters

5.3 Investigation of effects of noise on identification performance

The performance of the proposed method depends on the quality of the measured boundary force data, and full-field and boundary displacements obtained from digital image correlation. Since measurement error and noise will naturally be present in any experimental data, a simulation experiment was conducted to assess the effects of noise in both the loading data and the DIC displacement data. The simulation injects noise of practical levels in the synthetic data previously produced by FE simulation, and re-runs the proposed method with the noisy synthetic data. For this test, the verification case that used the open-hole test specimen under biaxial non-proportional loading is selected.

Image noise is usually in the form of undesirable random fluctuations of the brightness or color information in the color image produced by the CCD (Charge-Coupled Device) camera when it captures the images in a harsh environment. In the case of grayscale images, the noise presents in a form of variation of the gray level of a pixel from its true value; the gray level is a single number and carries the light intensity information at that pixel. Such image noises will degrade the quality of the image and could potentially impose difficulties to any DIC-based inverse identification algorithm. To assess the robustness of the proposed method in the presence of image noise, it is assumed that the images used to provide displacement information are corrupted by Gaussian noise, with different gray levels of noise at every pixel. The function used to introduce the noise (Besnard 2006) is

$$\sigma_u = \frac{12\sqrt{2}\sigma_g P}{7\langle |\nabla f|^2 \rangle^{1/2} l} \quad (24)$$

where σ_u is the standard deviation of the full-field displacements, due to the introduction of Gaussian noise in the pixel gray levels, σ_g is the standard deviation of the gray level, P is the physical pixel size, $\langle |\nabla f|^2 \rangle$ is a spatially averaged gradient of the gray level within the zone of interest (ZOI), and l is the smallest dimension of the ZOI, measured in pixels. From Eq. (24), it follows that the larger the size of a single pixel size, and the smaller the size of the ZOI, the larger the noise that will be introduced. The averaged gradient $\langle |\nabla f|^2 \rangle$ represents the averaged level of contrast of the image and in general, a small contrast level leads to a high noise level in an image. In this case, the minimum dimension of the ZOI is assumed to be 144 pixels and the physical pixel size is set to be 0.013889in/pixel. σ_u is shown in Fig. 12 as a function of the standard deviation of the gray level for different $\langle |\nabla f|^2 \rangle$ values. In practice, for most CCD cameras the noise level is characterized with a maximum range less than 3 gray levels. Therefore, $\sigma_g = 3$ is assumed for the image noise. The displacement fluctuations caused by the image noise has zero mean and standard deviation σ_u calculated by Eq. (24). These fluctuations are superimposed onto the synthetic full-field displacements to produce noisy displacement data.

In order to simulate the noise in the measured boundary force data, the synthetic loading data were also perturbed. It is notable that the measurement errors of most transducers depend on the full-rated output (FRO). Even though many manufacturers specify the linearity of their load cells as a percentage of the FRO, effects of the noise floor could be amplified if only a small fraction of the full loading capacity is utilized; for example, a load cell rated at 0.05% FRO produces a reading error of 5% at 1:100th of full scale. Thus, a load cell with proper capacity has to be chosen when setting up an experimental tested to reduce the propagation of uncertainty in the identification

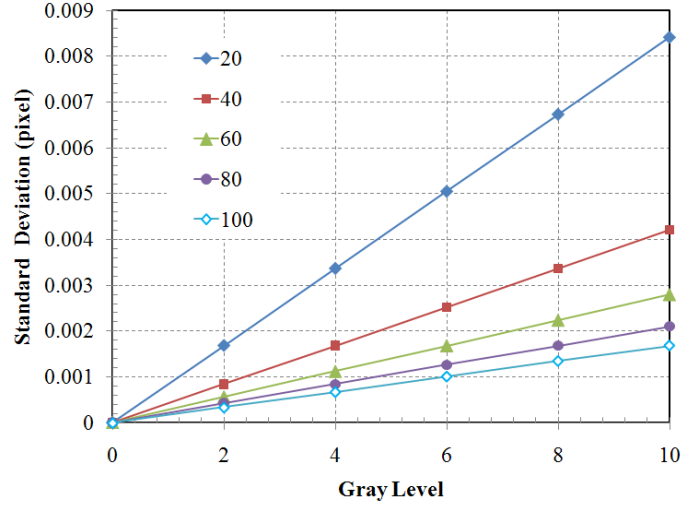


Fig. 12 Standard deviation (σ_u) of displacement field introduced by Gaussian noise verses gray level for different spatially averaged gradient values ($\langle |\nabla f|^2 \rangle = 20, 40, 60, 80$, and 100)

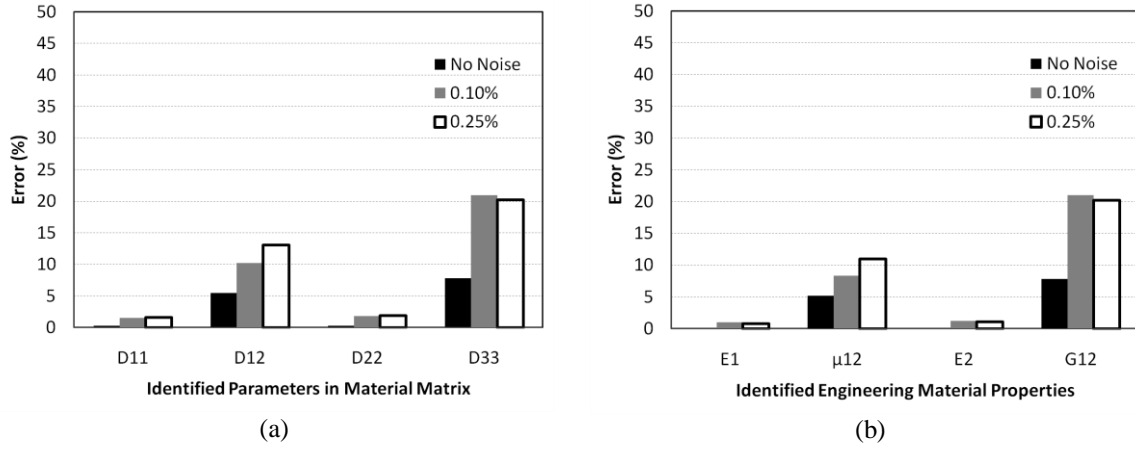


Fig. 13 Identified results represented by: (a) material constitutive parameters; (b) engineering material properties under image noises ($\sigma_u=0, 0.1\%$, and 0.25%) and the force measurement error ($\sigma_r=0.25\%$) in all three cases

method. In normal practice, the uncertainty (defined as 2.4 times the standard deviation) of the measurement error by the Class A load cell is less than 0.25% (ASTM 2006). Thus, for our experiment the synthetic load data at each load step were randomly perturbed with Gaussian noise with zero mean and standard deviation of $\sigma_r=0.25\%$ as a severe noisy case.

The errors in the parameters identified by the proposed method using noisy data are shown in Fig. 13. Three different image noise levels ($\sigma_u=0, 0.1\%$ and 0.25%) and load cell noise level ($\sigma_r=0.25\%$) are considered. The load cell noise is applied in all three tested cases. It is observed that the errors in the identified D_{11} and D_{22} are small. This implies that the proposed method can

identify material parameters in a way that is insensitive to the perturbation of the reference data, provided that the corresponding energy components are of reasonable size. The reason that the identification of D_{66} and D_{12} is relatively more sensitive to noise is that the fractions of the corresponding energy components W_{66} and W_{12} are marginal compared to the other energy components. Not surprisingly, relatively large error in D_{66} and D_{12} results from relatively large error in the Poisson ratio μ_{21} and shear modulus G_{12} which are backcalculated from the identified material stiffness values.

6. Conclusions

In this paper, we present a novel inverse identification method for material characterization based on two-dimensional digital image correlation. In contrast with conventional material characterization methods using strain gages, which can characterize material properties only at specific points, the proposed method can obtain the averaged material properties for an entire region of the specimen. A primary difference from existing identification methods is that the proposed method does not need to solve boundary value problems of the target specimens using recursively updated parameters; in this sense, the method is free of finite element analysis (FEA). Unlike the VFM, the proposed method ensures that the computed stress fields are statically admissible by basing them on the true DIC displacement fields. For this purpose, the equilibrium is enforced by selecting polynomial terms that satisfy the strong form of the equilibrium equations and nodal force equilibrium conditions. The element-by-element approach has the advantage that it is less memory-intensive than approaches that need to assemble large system matrices for the entire finite element model. The method also allows flexibility in the choice of the polynomial order of the stress field approximations, depending on the element size and stress gradients. The approach explicitly enforces the equilibrium conditions based on the true DIC displacements, and minimization of the objective function in terms of the energy principle also implicitly enforces traction and displacement boundary conditions.

The presented method has been validated in simulation using a set of synthetic data based on finite element simulation of specimens made of materials having isotropic and orthotropic properties. The effect of loading conditions (i.e., proportional and non-proportional loadings) on the performance of the identification method has been investigated, as has the role that the specimen geometry plays in generating the different non-uniform stress fields needed for identification. The method is shown to successfully find the parameters of the material constitutive matrix. Energy component analysis is used to give insight into why some parameters are identified with less error than others, and further, to provide guidance for the design of the experiments. Experimental noise inherent in capturing images and measuring loadings are considered in order to verify the robustness of the proposed method in the presence of noise. Three material properties (E_1 , E_2 and μ_{12}) could be accurately identified in the presence of reasonable and practical levels of noise. Although G_{12} shows relatively higher sensitivity to the noise than the other parameters, its sensitivity could be potentially improved by design of optimal experiments. The loading direction and the specimen geometry are seen to have significant influence on the performance of the method for identification of composite material; the design of optimal experiments, i.e., the consideration of optimal specimen geometry and loading paths, will be addressed in the further research.

Acknowledgements

This research is supported by the New Faculty Startup Fund from the University of Akron. The authors are grateful for this support.

References

- ASTM (2006), ASTM E74-06 Standard Practice of Calibration of Force-Measuring Instruments for Verifying the Force Indication of Testing Machines, ASTM.
- Avril, S., Bonnet, M., Bretelle, A.S., Grediac, M., Hild, F., Ienny, P., Latourte, F., Lemosse, D., Pagano, S., Pagnacco, E. and Pierron, F. (2008), "Overview of identification methods of mechanical parameters based on full-field measurements", *Experimental Mechanics*, **48**(4), 381-402.
- Avril, S., Grediac, M. and Pierron, F. (2004), "Sensitivity of the virtual fields method to noisy data", *Computational Mechanics*, **34**(6), 439-452.
- Avril, S., Huntley, J.M., Pierron, F. and Steele, D.D. (2008), "3D heterogeneous stiffness reconstruction using MRI and the virtual fields method", *Experimental Mechanics*, **48**(4), 479-494.
- Avril, S. and Pierron, F. (2007), "General framework for the identification of constitutive parameters from full-field measurements in linear elasticity", *International Journal of Solids and Structures*, **44**(14-15), 4978-5002.
- Avril, S., Pierron, F., Pannier, Y. and Rotinat, R. (2008), "Stress reconstruction and constitutive parameter identification in plane-stress elasto-plastic problems using surface measurements of deformation fields", *Experimental Mechanics*, **48**(4), 403-419.
- Besnard, N., Hild, F. and Roux, S. (2006), "Finite-element displacement fields analysis from digital images: application to portevin-le Chtelier bands", *Experimental Mechanics*, **46**(6), 789-803.
- Calderon, A.P. (1980), "On an Inverse Boundary Value Problem", *Seminar on Numerical Analysis and Its Applications to Continuum Physics*, Rio de Janeiro.
- Chalal, H., Avril, S., Pierron, F. and Meraghni, F. (2006), "Experimental identification of a nonlinear model for composites using the grid technique coupled to the virtual fields method", *Composites Part a-Applied Science and Manufacturing*, **37**(2), 315-325.
- Claire, D., Hild, F. and Roux, S. (2004), "A finite element formulation to identify damage fields: the equilibrium gap method", *International Journal for Numerical Methods in Engineering*, **61**(2), 189-208.
- Constantinescu, A. and Tardieu, N. (2001), "On the identification of elastoviscoplastic constitutive laws from indentation tests", *Inverse Problems in Engineering*, **9**(1), 19-44.
- Crouzeix, L., Perie, J.N., Collombet, F. and Douchin, B. (2009), "An orthotropic variant of the equilibrium gap method applied to the analysis of a biaxial test on a composite material", *Composites Part a-Applied Science and Manufacturing*, **40**(11), 1732-1740.
- Furukawa, T. and Michopoulos, J.G. (2008a), "Computational design of multiaxial tests for anisotropic material characterization", *International Journal for Numerical Methods in Engineering*, **74**(12), 1872-1895.
- Furukawa, T. and Michopoulos, J.G. (2008b), "Online planning of multiaxial loading path for elastic material identification", *Computer Methods in Applied Mechanics and Engineering*, **197**(9-12), 885-901.
- Furukawa, T., Michopoulos, J.G. and Kelly, D.W. (2008), "Elastic characterization of laminated composites based on multiaxial tests", *Composite Structures*, **86**(1-3), 269-278.
- Geymonat, G. and Pagano, S. (2003), "Identification of mechanical properties by displacement field measurement: a variational approach", *Meccanica*, **38**(5), 535-545.
- Grediac, M. and Pierron, F. (2006), "Applying the virtual fields method to the identification of elasto-plastic constitutive parameters", *International Journal of Plasticity*, **22**(4), 602-627.
- Grediac, M., Pierron, F., Avril, S. and Toussaint, E. (2006), "The virtual fields method for extracting constitutive parameters from full-field measurements: a review", *Strain*, **42**(4), 233-253.

- Grediac, M. and Vautrin, A. (1990), "A new method for determination of bending rigidities of thin anisotropic plates", *Journal of Applied Mechanics-Transactions of the Asme*, **57**(4), 964-968.
- Hild, F. and Roux, S. (2006), "Digital image correlation: from displacement measurement to identification of elastic properties - a review", *Strain*, **42**(2), 69-80.
- Kajberg, J. and Lindkvist, G. (2004), "Characterization of materials subjected to large strains by inverse modelling based on in-plane displacement fields", *International Journal of Solids and Structures*, **41**(13), 3439-3459.
- Kajberg, J. and Wikman, B. (2007), "Viscoplastic parameter estimation by high strain-rate experiments and inverse modeling - speckle measurements and high-speed photography", *International Journal of Solids and Structures*, **44**(1), 145-164.
- Latourte, F., Chrysochoos, A., Pagano, S. and Wattrisse, B. (2008), "Elastoplastic behavior identification for heterogeneous loadings and materials", *Experimental Mechanics*, **48**(4), 435-449.
- Lecompte, D., Smits, A., Sol, H., Vantomme, J. and Van Hemelrijck, D. (2007), "Mixed numerical-experimental technique for orthotropic parameter identification using biaxial tensile tests on cruciform specimens", *International Journal of Solids and Structures*, **44**(5), 1643-1656.
- Mahnken, R. (2000), "A comprehensive study of a multiplicative elastoplasticity model coupled to damage including parameter identification", *Computers & Structures*, **74**(2), 179-200.
- Moreau, A., Pagnacco, E., Borza, D. and Lemosse, D. (2006), "An evaluation of different mixed experimental/numerical procedures using FRF for the identification of viscoelastic materials", *International conference on noise and vibration engineering ISMA*, Leuven.
- Pagnacco, E., Lemosse, D., Hild, F. and Amiot, F. (2005). "Inverse strategy from displacement field measurement and distributed forces using FEA", *SEM Annual Conference and Exposition on Experimental and Applied Mechanics*, Poland.
- Pierron, F., Vert, G., Burguete, R., Avril, S., Rotinat, R. and Wisnom, M.R. (2007), "Identification of the orthotropic elastic stiffnesses of composites with the virtual fields method: sensitivity study and experimental validation", *Strain*, **43**(3), 250-259.
- Regez, B., Zhang, Y., Chu, T.C., Don, J. and Mahajan, A. (2008), "In-plane bulk material displacement and deformation measurements using digital image correlation of ultrasonic C-scan images", *Structural Engineering and Mechanics*, **29**(1), 113-116.
- Wilson, E.L. and Ibrahimbegovic, A. (1990), "Use of incompatible displacement modes for the calculation of element stiffnesses or stresses", *Finite Elements in Analysis and Design*, **7**(3), 229~241.
- Yun, G.J., Ogorzalek, K.A., Dyke, S.J. and Song, W. (2009), "A two-stage damage detection approach based on subset of damage parameters and genetic algorithms", *Smart Structures and Systems*, **5**(1), 1-21.